Cubic to Tetragonal Phase Transition in $CuFe_2O_4$ Nanoparticles

Shanigaram Mallesh, Minji Gu, and Ki Hyeon Kim*

Department of Physics, Yeungnam University, Gyeongsan 38541, Republic of Korea

We report the influence of annealing temperature (600 °C-1000 °C) on structure, crystallographic phase transition, morphology, vibrational, and magnetic properties of $CuFe_2O_4$ nanoparticles synthesized by a facile sol-gel auto combustion technique. The as-prepared and 600 °C air annealed samples show cubic spinel structure, secondary phases of α-Fe_2O_3, and CuO (minute reflections), resulting in inferior magnetic properties. Further, the 800 °C air annealed sample discloses a structural phase transition from cubic to tetragonal phase and minute α-Fe_2O_3 secondary phase. This sample exhibits the highest coercivity (H_C) 1221.4 Oe and squareness ratio (M_R/M_{20kOe}) = 0.56. On the other hand, the sample annealed at 1000 °C in air reveals superior magnetic properties (magnetization = 24.5 emu/g & H_C = 484.7 Oe) compared to all other samples. The revolution of magnetic properties with annealing temperature originates from the morphology, cubic to a tetragonal structural phase transition, c/a > 1, and cation site occupation induced by Jahn–Teller distortion.

Keywords : $CuFe_2O_4$ nanoparticles, structural phase transition, microstructure, magnetization, coercivity

1. Introduction

Among several spinel ferrites, copper ferrite ($CuFe_2O_4$) has gained considerable attention owing to its intriguing structural, optical, electrochemical, and magnetic properties [1, 2]. These properties are worthwhile in various potential applications, including water treatment, catalysis, gas sensors, lithium-ion batteries, and biological applications [2-6]. The physical/chemical properties of $CuFe_2O_4$ nanostructures are strongly affected by structure, morphology (shape, size, & size distribution), and the cation distribution in their definite magnetic sites [7-9]. $CuFe_2O_4$ exists in two crystallographic phases: the high-temperature (T > 700 K) cubic spinel phase (c-$CuFe_2O_4$, lattice parameter 8.38 Å, space group: Fd-3m) and the low-temperature (T < 700 K) tetragonal phase (t-$CuFe_2O_4$, lattice parameters a = 5.82 Å, c = 8.71 Å, space group: $I4_1$/amd) based on preparation methods and annealing conditions [10, 11]. The structural transition from high symmetry cubic (Fd-3m) to low symmetry tetragonal ($I4_1$/amd) is caused by Jahn–Teller distortion. In an ideal unit cell configuration, eight divalent Cu^{2+} ions occupy the octahedral site (B), and 16 trivalent Fe^{3+} are equally

distributed in tetrahedral (A) and B sites [12]. The magnetic moment of sublattice-A is antiparallel to sublattice-B. Therefore, the total effective magnetic moment (μ_{eff}) of $CuFe_2O_4$ originates from the unbalanced magnetic moments of eight Cu^{2+} ions in sublattice-B [13, 14]. Therefore, it possesses ferrimagnetic behavior with Néel temperature of nearly 780 K [13, 14]. Several groups have been synthesized the $CuFe_2O_4$ samples using bottom-up and top-down methods and observed structural phase transition from cubic to tetragonal or vice versa by applying heat treatments and varying the processing conditions. Goya *et al.* observed tetragonal to cubic phase transition in a bulk $CuFe_2O_4$ reduced by a high-energy ball milling method [15]. Yadav *et al.* synthesized $CuFe_2O_4$ NPs using glucose and fructose (honey) assisted sol-gel process. They have observed cubic to tetragonal phase transition and the CuO secondary phase with an increased annealing temperature of as-prepared NPs from 500 °C to 1100 °C [16]. Laokul *et al.* synthesized $CuFe_2O_4$ NPs using aloe vera in the sol-gel process, have seen cubic phase and secondary phase of CuO in sample annealed at 600 °C, which is transformed to a tetragonal phase when annealed at 900 °C [17]. Therefore, the above reports showed that the structure, phase transition, cationic site occupation, and magnetic properties are sensitive to heat treatments and processing conditions.

Herein, we have synthesized the $CuFe_2O_4$ nanoparticles

*Corresponding author: Tel: +82-53-810-2334
Fax: +82-53-810-4616, e-mail: kee1@ynu.ac.kr

(NPs) by the simple triethylamine-assisted sol-gel process. The as-prepared NPs have been subjected to heat-treatment in a temperature range of 600 °C to 1000 °C in air to study the structure and magnetic properties. XRD analysis revealed cubic to tetragonal phase transition with the increased annealing temperature. The evaluated lattice parameters and the value of c/a > 1 indicate that the structural phase transition is due to the Jahn–Teller distortion in annealed (800 °C & 1000 °C) samples. Raman spectra further confirm the cubic to tetragonal phase transition with the rising of annealing temperature. The magnetic properties of $CuFe_2O_4$ NPs were improved with the increase of annealing temperature due to the rise in crystallite/particle size, decreased surface disorder, and a change in cation distribution induced by Jahn–Teller distortion.

2. Experimental Details

Figure 1 demonstrates the synthesis and growth of morphology corresponding to the crystallographic phase transition (different color powder samples shown in insets) with annealing temperature. The $CuFe_2O_4$ NPs were prepared by the sol-gel route starting with $CuSO_4 \cdot 5H_2O$ and $Fe(NO_3)_3 \cdot 9H_2O$ salts as for the erstwhile work on MnZn ferrite NPs [20]. The required amount of precursors solvated in 15 ml of ethylene glycol, and subsequently, 20-25 drops of glycerol were added to stabilize the solution at 75 °C. The vigorous magnetic stirring continued until the formation of a homogeneous solution. The solution was brought to room temperature and further

dissolved in 37 ml of 2-propanol & 18 ml triethylamine and stirring proceeded for 15 minutes to obtain the gel. Lastly, the brown color gel burnt at 180 ºC for several hours to acquire the final product (Fig. 1). The as-prepared (*AP*) NPs were heat-treated in temperatures from 600 ºC-1000 ºC to study structural and magnetic properties. The X-ray diffraction (XRD) data procured with PANalytical X'pert PRO, CuKα (λ = 1.54059 Å) radiation. Vibrational properties examined using Raman spectra (Jobin-Yvon LabRAM HR800UV) with He-Ne laser of 633 nm. The morphology of the samples was analyzed using field emission scanning electron microscopy (FESEM, Hitachi, S-4800). The vibrating sample magnetometer (VSM, Microsense EV9) was used to study the magnetic properties at room temperature.

3. Results and Discussions

Figure 2 shows the XRD patterns of the $CuFe_2O_4$ *AP* and air annealed (600 °C-1000 °C) samples, respectively. The *AP* NPs unveils the cubic spinel phase (JCPDS 77-0010) and a minor quantity of secondary phases corresponding to the α-Fe_2O_3 (JCPDS 33-0664) and CuO (very small). The sample annealed at 600 °C also shows the cubic spinel phase and secondary phase (α-Fe_2O_3), with increased secondary phase intensity than the *AP* sample due to the increased oxidation. These observations are similar to the earlier reports on $MgFe_2O_4$, Fe_3O_4, and $MnZnFe_2O_4$ cubic spinel structures annealed under similar conditions [18-20]. Further cubic to tetragonal phase transition appeared in sample annealed at 800 °C with
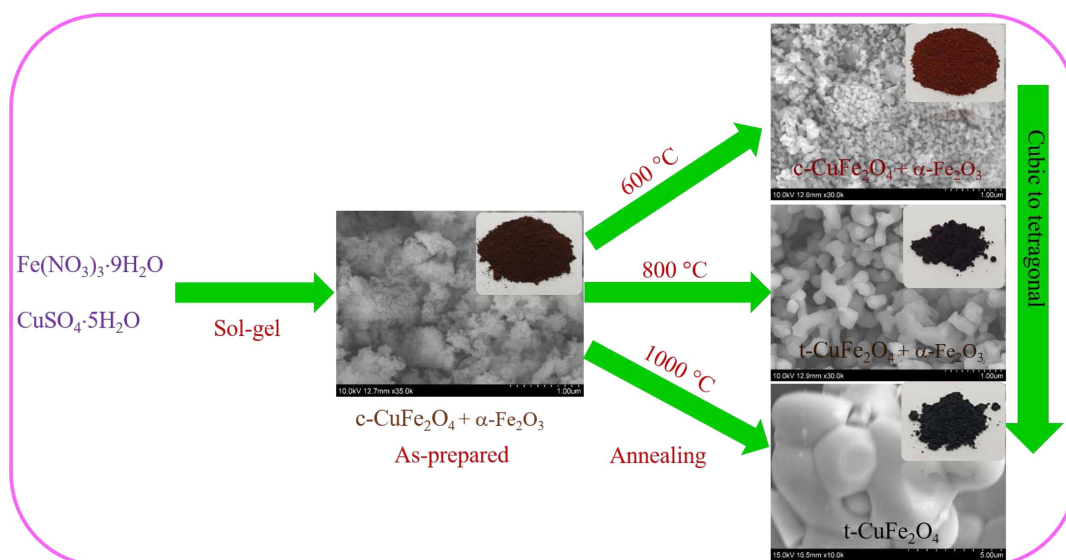
Fig. 1. (Color online) Schematic representation for the synthesis of $CuFe_2O_4$ nanoparticles, the growth of morphology (the different colored powder samples were shown in insets), and corresponding structural phase transition with the increase of annealing temperature.
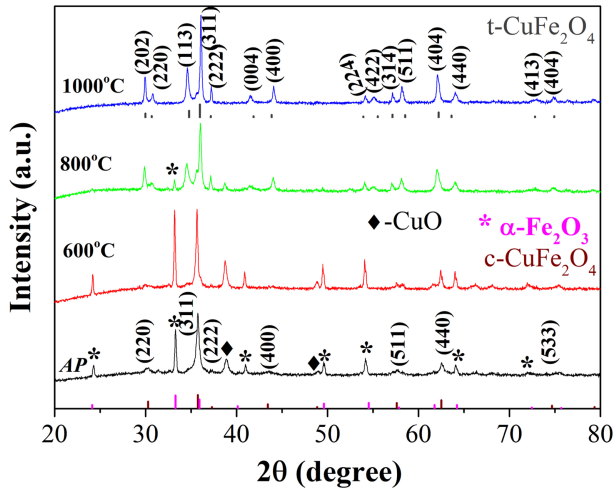
Fig. 2. (Color online) XRD patterns of as-prepared and air annealed $CuFe_2O_4$ samples.

significantly reduced secondary phase fraction. On the other hand, the pure tetragonal phase (JCPDS 35-0425) is realized in the sample annealed at 1000 °C. Therefore, annealing at higher temperatures leads to developing a tetragonal phase in $CuFe_2O_4$ cubic spinels [16, 17]. The sharper peaks seen in high-temperature annealed samples indicate that the rise of crystallite size. Therefore, the crystallite size was determined by XRD peak width of highest intensity peak (311) using the Scherrer formula for *AP* and annealed samples. The crystallite size is 23.7 nm for *AP* NPs, increasing with annealing temperature and reaching a value of 60.7 nm for 1000 °C annealed sample (see Table 1). Lattice parameters and c/a ratio values calculated using the relation for cubic phase [16, 22]

$$1/d^2 = h^2 + k^2 + l^2/a^2 \qquad (1)$$

and for the tetragonal phase

$$1/d^2 = h^2 + k^2 / a^2 + l^2/c^2 \qquad (2)$$

where d is the interplanar distance, a and c are lattice parameters, and (hkl) is the miller indices.

The evaluated lattice parameters and c/a ratio values have summarized in Table 1. The lattice parameter a value for cubic $CuFe_2O_4$ spinels are 8.3211 Å and 8.3483 Å for *AP* and 600 °C air annealed samples, respectively. The observed values are in good agreement with earlier reports [12, 22]. As shown in Table 1, for the tetragonal phase, the a (=b) value slightly decreased with the increase of annealing temperature, but, c value and c/a ratio increased with the increase of annealing temperature. Therefore, cubic to tetragonal phase transition is due to the Jahn–Teller effect related to cation redistribution and the value of c/a [16]. The structural variation associated with cation redistribution and the value of c/a could lead to a development in magnetic properties.

Raman spectroscopy is a powerful technique to study the structure, phase formations, and vibrational properties of the samples. Fig. 3(a) depicts the frequency (100-1000 cm^{-1}) dependent Raman spectra of $CuFe_2O_4$ *AP* and air annealed (600 °C-1000 °C) samples at room temperature. In ambient conditions, cubic spinel structures exhibit five Raman active modes ($A_{1g}+E_g+3T_{2g}$) [18]. Fig. 3(b, c) shows the Raman modes observed around A_{1g} (217 cm^{-1}) and $4E_g$ (241 cm^{-1}, 289 cm^{-1}, 406 cm^{-1} & 604 cm^{-1}), which belong to the secondary phase of α-Fe_2O_3 of *AP* and 600 °C annealed samples [21]. The Raman modes observed at 498 cm^{-1} [$T_{2g}(3)$] and 652 cm^{-1} [A_{1g}] correspond to the cubic spinel phase [16]. The absence of other ferrite modes at lower frequency regions might be due to the overlapping with the α-Fe_2O_3 modes. On the other hand, Raman modes were split for 800 C and 1000 °C

Table 1. The structural and magnetic parameters. Where t is the crystallite size, 'a, c' are the lattice parameters, D is the particle diameter. M_{20kOe}, M_R, and Hc are the magnetization obtained at 20 kOe, remanent magnetization, and coercivity.

Samples	*AP*	600 °C	800 °C	1000 °C
t (nm)	23.7	36.1	46.4	60.7
Phase	c-$CuFe_2O_4$ + α-Fe_2O_3 + CuO (minute)	c-$CuFe_2O_4$ + α-Fe_2O_3 + CuO (minute)	t-$CuFe_2O_4$ + α-Fe_2O_3 (minute)	t-$CuFe_2O_4$
a (Å)	8.3211	8.3483	8.2264	8.2094
c (Å)	-	-	8.6972	8.7133
c/a	-	-	1.054	1.062
D (nm)	38.7	66.1	420	4.2 (μm)
M_{20kOe} (emu/g)	12.4	5.7	21.2	24.5
M_R (emu/g)	3.2	2.5	11.8	12.5
M_R/M_{20kOe}	0.26	0.44	0.56	0.47
Hc (Oe)	247.4	1018	1221.4	484.7
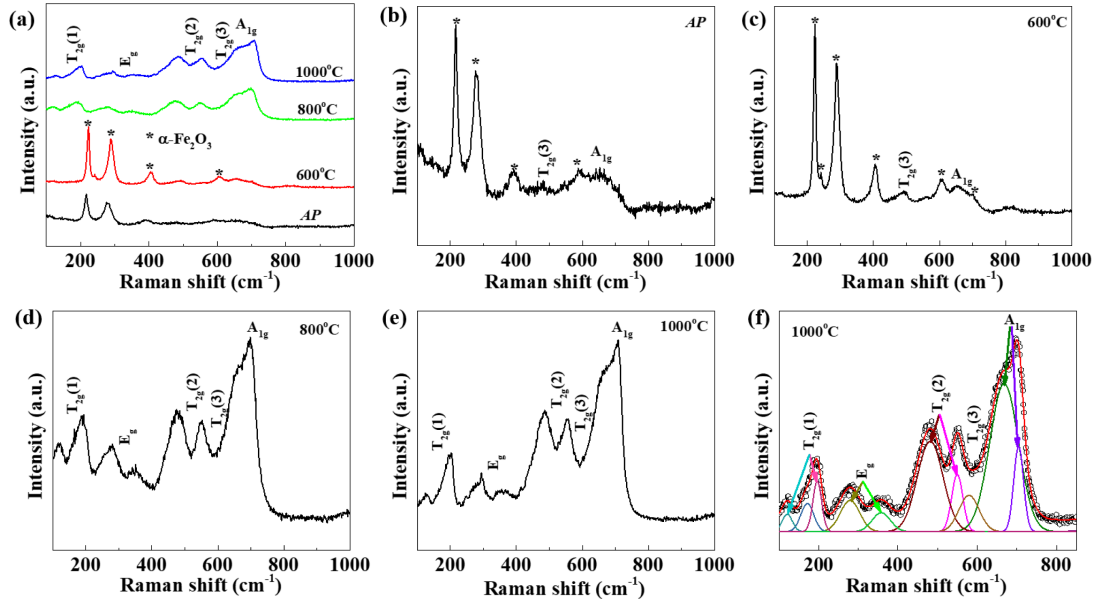
Fig. 3. (Color online) Raman spectra of as-prepared and air annealed CuFe$_2$O$_4$ samples.

annealed samples due to the presence of the tetragonal phase. Fig. 3(d, e) presents the Raman modes observed at A$_{1g}$ (664 cm^{-1} & 703 cm^{-1}), 3T$_g$ (582 cm^{-1}, 493 cm^{-1} & 548 cm^{-1}, 122 cm^{-1} & 196 cm^{-1}) and E$_g$ (277 cm^{-1} & 361 cm^{-1}) for 800 °C and 1000 °C samples, which is consistent to the tetragonal inverse spinel ferrites phase. The cubic to tetragonal structural phase transition is due to the Jahn-Teller distortion [16, 22]. Fig. 3(f) displays the Lorentzian fit to the Raman spectra for 1000 °C annealed sample to attain the natural band positions, as shown in Table 1. Therefore, the Raman spectroscopy study further confirms the structural phase transition from cubic to tetragonal phase with increased annealing temperature, which justifies the XRD results.

Figure 4 illustrates the FESEM images and histograms of the *AP* and air annealed CuFe$_2$O$_4$ samples. The particle size distribution obtained from FESEM images, as shown in size histograms. The morphology of the *AP* NPs exhibits a nearly sphere-shaped with the average particle is 38.7 nm, as displayed in Fig. 4(a-c). In the 600 °C annealed sample, the average particle size is slightly increased to 66.1 nm, as revealed in Fig. 4(d-f). The particle size is increased to 420 nm for 800 °C annealed sample as shown in Fig. 4(g-i) due to aggregation of NPs. Further, growing the annealing temperature, the NPs accumulated and grown-up into bulk, which exhibits the polyhedral structure with an average size of 4.2 μm, as displayed in Fig. 4(j-l). The FESEM analysis divulges a remarkable effect on the morphologies of the NPs with the increase in annealing temperature. Further, Energy dispersive X-ray pattern and elemental mapping for the *AP* sample confirm

Cu, Fe, and O elements as presented in Fig. 5.

Figure 6(a, b) displays magnetic field-dependent magnetization (M-H curves) at room temperature RT for *AP* and air annealed CuFe$_2$O$_4$ samples. All samples exhibited ferrimagnetic behavior. It is observed that the magnetization of the 1000 °C annealed sample is found to be enhanced compared to all other samples. The measured values of magnetization (M) at 20 kOe, remanent magnetization (M$_R$), and coercivity (Hc) of *AP* and air annealed CuFe$_2$O$_4$ samples are presented in Table 1. The M of *AP* sample is 12.4 emu/g, which is decreased to 5.7 emu/g for the 600 °C annealed sample; then it again increased to 21.2 emu/g for the 800 °C annealed sample. Finally, it reached a maximum value of 24.5 emu/g for the 1000 °C annealed sample. The *AP* and 600 °C samples revealed lower magnetization than the samples annealed at 800 °C and 1000 °C, which can be ascribed to the secondary phases, finite-size, and surface effects. The randomly oriented surface spins (magnetic dead layer) on the surface of the NPs disturb the magnetic structure leading to a change in the magnitude of magnetization with a change in particle size in nanocrystalline samples. On the other hand, the improved magnetization at 1000 °C annealed sample is due to the pure t-CuFe$_2$O$_4$ phase and reduced surface defects. The magnetization increases with an increase in crystallite size due to the change in cation distribution with the increase of annealing temperature [22, 23]. However, the obtained M values of *AP* and air annealed samples were smaller than the bulk values (55 emu/g in c-CuFe$_2$O$_4$ and 49.7 emu/g in t-CuFe$_2$O$_4$) [25]. M value decreases due to the surface effects and change
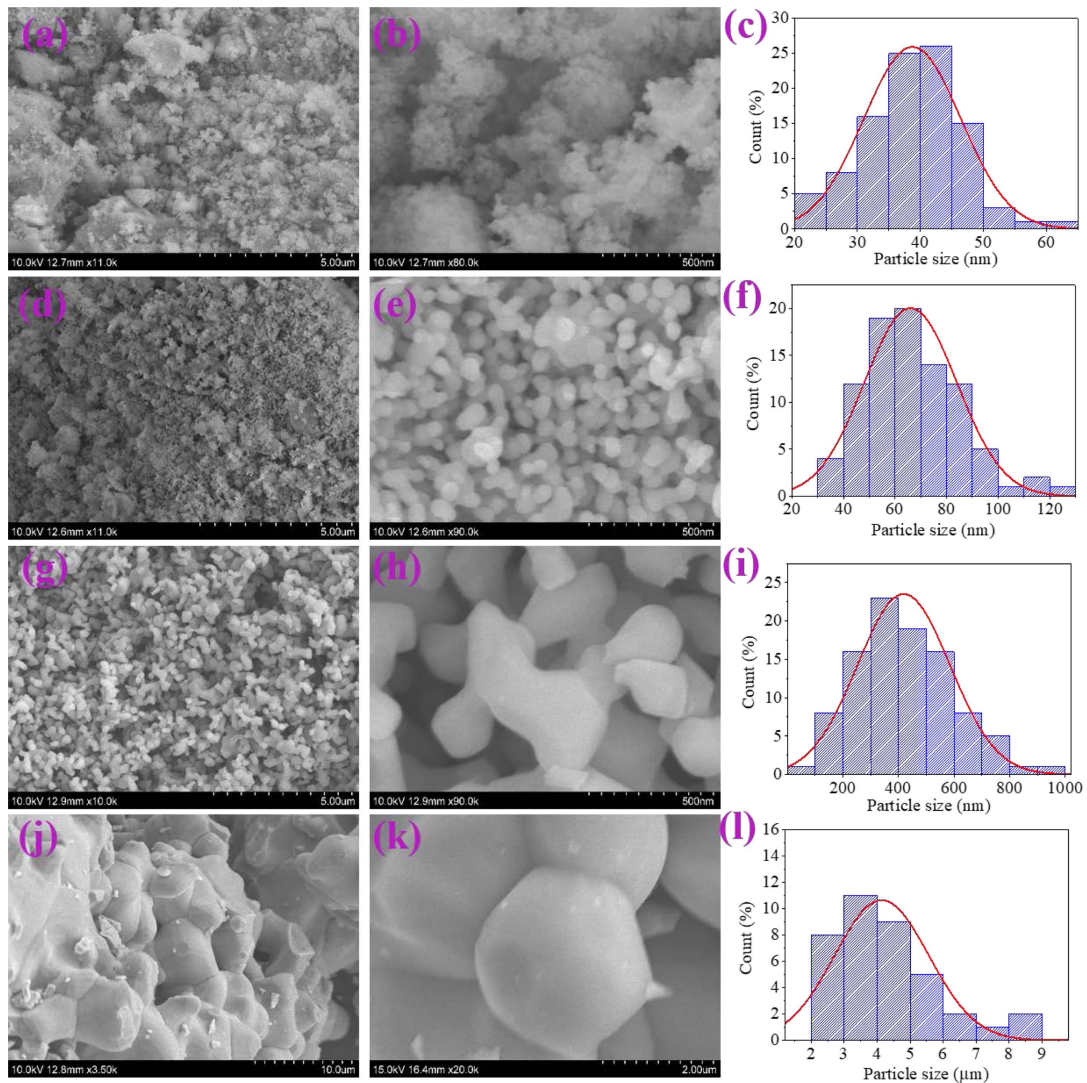
Fig. 4. (Color online) FESEM images of as-prepared and air annealed CuFe$_2$O$_4$ samples.
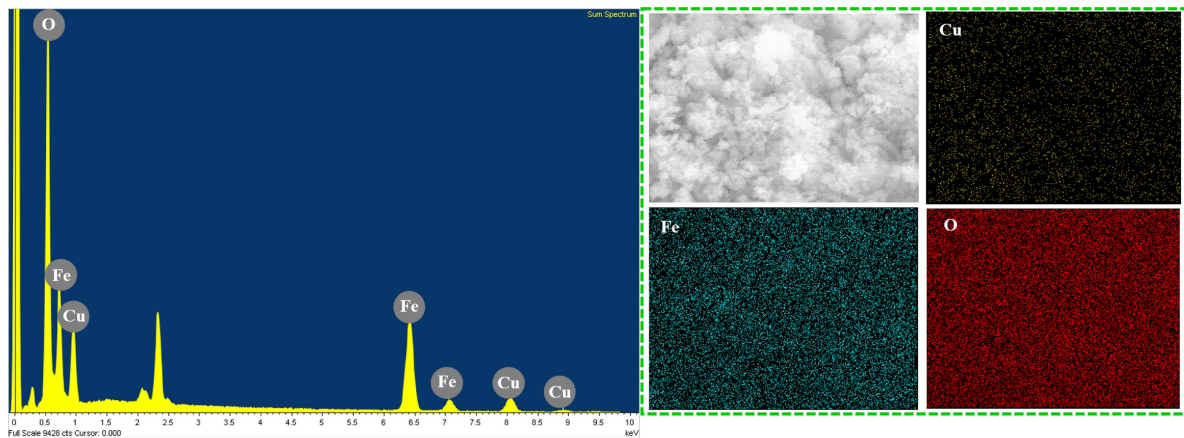
Fig. 5. (Color online) EDX pattern and element mapping of as-prepared CuFe$_2$O$_4$ nanoparticles.

in cationic distribution with reduced size in nanocrystals. In ferrites, the net magnetization originates from an antiparallel alignment of tetrahedral and octahedral sites. The relative distribution of Fe^{3+} and Cu^{2+} spins between
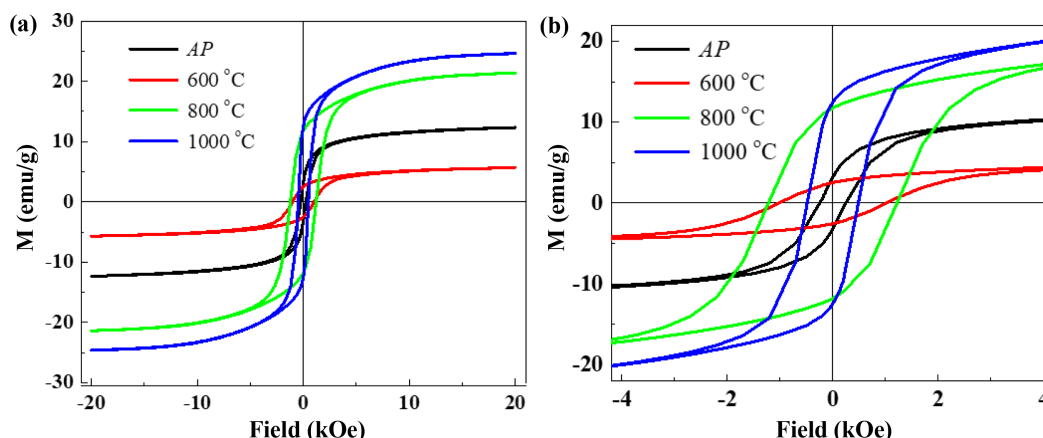
Fig. 6. (Color online) Isothermal M-H curves of as-prepared and air annealed $CuFe_2O_4$ samples.

tetrahedral and octahedral sites causes a change in magnetic moment. In bulk $CuFe_2O_4$, the net magnetic moment is observed due to 8 Cu^{2+} spins at octahedral sites [25]. Therefore, the partial decrease of Cu^{2+} spins at octahedral sites can reduce the magnetic moment in the annealed samples compared to bulk samples.

The value of Hc is 247.4 Oe, for the *AP* sample, which increased to a maximum value of 1221.4 Oe for the 800 °C annealed samples due to the size effects, microstructure, and presence of mixed-phase (t-$CuFe_2O_4$ and secondary phase). Further, Hc declines to below 484.7 Oe for 1000 °C annealed sample due to increased size and lessened surface effects. Moreover, the grain boundary condition changes noticeably with the increase of annealing temperature, and so the number of domain walls decreases as the annealing temperature increases. This behavior plays one of the most vital roles with the variation in Hc with annealing temperature. The squareness ratio (M_R/M_{20kOe}) for *AP* and annealed samples is shown in Table 1. The value of M_R/M_{20kOe} is 0.56 observed for the 800 °C annealed sample. This value is in agreement with bulk $CuFe_2O_4$ samples [24]. Therefore, the magnetic properties correlated with microstructural data suggest that the annealing temperature plays a significant role in cubic to the tetragonal structural phase transition.

4. Conclusions

In conclusion, the $CuFe_2O_4$ NPs were successfully synthesized by a simple sol-gel method. The influence of annealing temperature (600 °C-1000 °C) on microstructure, structural phase transition, and magnetic properties has been examined. The XRD and Raman spectra confirmed the cubic to tetragonal phase transition with an increase of annealing temperature. FESEM analysis revealed that the

size of *AP* (38.7 nm), which reached to a bulk value (4.2 μm) when annealed at 1000 °C. The *AP* and 600 °C samples exhibited weak magnetic properties owed to the secondary phase α-Fe_2O_3. On the other hand, the sample annealed at 1000 °C displayed a single-phase tetragonal inverse spinel phase with superior magnetic properties (M = 24.5 emu/g, Hc = 484.7 Oe) attributed to the larger size, Jahn–Teller distortion, and change cation site occupation.

References

[1] A. Goldman, Modern ferrite technology, Springer, Pittsburg (2006).

[2] N. Masunga, O. K. Mmelesi, K. K. Kefeni, and B. B. Mamba, J. Environ. Chem. Eng. **7**, 103179 (2019).

[3] A. Maleki, Z. Hajizadeh, and P. Salehi, Sci. Rep. **9**, 5552 (2019).

[4] A. Singh, A. Singh, S. Singh, and P. Tandon, Sens. Actuators B **244**, 806 (2017).

[5] L. Jin, Y. Qie, H. Deng, W. Li, H. Li, and S. Yang, Electrochim. Acta **56**, 9127 (2011).

[6] H.-M. Fan, J.-B. Yi, Y. Yang, K.-W. Kho, H.-R. Tan, Z.-X. Shen, J. Ding, X.-W. Sun, M. C. Olivo, and Y.-P. Feng, ACS Nano **3**, 2798 (2009).

[7] M-A, Kar, R. Fazaeli, F. Manteghi, and M. Ghahari, Environ. Prog. Sustain. Energy **38**, 13107 (2019).

[8] B. K. Chatterjee, K. Bhattacharjee, A. Dey, C. K. Ghosh, and K. K. Chattopadhyay, Dalton Trans. **43**, 7930 (2014).

[9] Z. Huang, Y. Zhu, S. Wang, and G. Yin, Cryst. Growth.

Design. **6**, 1931 (2006).

[10] M. D. P. Silva, F. C. Silva, F. S. M. Sinfronio, A. R. Paschoal, E. N. Silva, and C. W. A. Paschoal, J. Alloys. Compd. **584**, 573 (2014).

[11] T. P. Sumangala, C. Mahender, A. Barnabe, N. Venkataramani, and S. Shiva Prasad, J. Magn. Magn. Mater. **418**, 48 (2016).

[12] D. Thapa, N. Kulkarni, S. N. Mishra, P. L. Paulose, and P. Ayyub, J. Phys. D: Appl. Phys. **43**, 195004 (2010).

[13] A. M. Balagurov, I. A. Bobrikov, V. Y. Pomjakushin, D. V. Sheptyakov, and V. Y. Yushankhai, J. Magn. Magn. Mater. **374**, 591 (2015).

[14] B. J. Evans and S. S. Hafner, J. Phys. Chem. Solids **29**, 1573 (1968).

[15] G. F. Goya, H. R. Renchenberg, and J. Z. Jiang, J. Appl. Phys. **84**, 1101 (1998).

[16] R. S. Yadav, I. Kuritka, J. Vilcakova, J. Havlica, J. Masilko, L. Kalina, J. Tkacz, M. Hajduchova, and V. Enev, J. Mater. Sci: Mater Electron. **28**, 6245 (2017).

[17] P. Laokul, V. Amornkitbamrung, S. Seraphin, and S. Maensiri, Curr. Appl. Phys. **11**, 101 (2011).

[18] S. Mallesh and K. H. Kim, J. Magn. **24**, 650 (2019).

[19] A. Jafari, S. F. Shayesteh, M. Salouti, and K. Boustani, J. Magn. Magn. Mater. **379**, 305 (2015).

[20] S. Mallesh and V. Srinivas, J. Magn. Magn. Mater. **475**, 290 (2019).

[21] S. Mallesh, D. Narsimulu, and K. H. Kim, Phys. Lett. A **384**, 126038 (2020).

[22] R. S. Yadav, J. Havlica, J. Masilko, L. Kalina, J. Wasserbauer, M. Hajduchova, V. Enev, I. Kurtika, and Z. Kozakova, J. Supercond. Nov. Magn. **29**, 759 (2016).

[23] N. K. Thanh, T. T. Loan, L. N. Anh, N. P. Duong, S. Soontaranon, N. Thammajak, and T. D. Hien J. Appl. Phys. **120**, 142115 (2016).

[24] J. Zhao, Y. Cheng, X. Yan, D. Sun, F. Zhu, and Q. Xue, Cryst. Eng. Comm. **14**, 5879 (2012).

[25] S. Roy and J. Ghose, J. Appl. Phys. **87**, 6226 (2000).